buildings

MDPI

Article

Electrical Characteristics and Desaturation Effectiveness During Horizontal Electrolysis in Calcareous Sand

Yumin Chen [1,2,*], Ying Zhou [1], Runze Chen [2], Saeed Sarajpoor [3] and Xiao Xie [1]

[1] College of Civil and Transportation, Hohai University, Nanjing 210024, China; yingzhouhhu@hhu.edu.cn (Y.Z.); xiexiao@hhu.edu.cn (X.X.)
[2] School of Civil Engineering, Suzhou University of Science and Technology, Suzhou 215011, China; chen95@usts.edu.cn
[3] Institute for Smart City of Chongqing University in Liyang, Chongqing University, Changzhou 213300, China; sarajpoor@163.com
* Correspondence: ymch@hhu.edu.cn

Abstract: Electrolysis desaturation has emerged as an innovative technique to mitigate liquefaction risk by reducing soil saturation in liquefiable foundations. This study evaluated the effectiveness of horizontal electrolysis on calcareous sandy foundations in marine environments by employing 35‰ NaCl solution as pore fluid under different current intensities (1A, 2A, and 4A). Experimental results demonstrated that hydrogen gas was generated at the cathode, while chlorine gas was produced at the anode, with peak gas retention rates of 100%, 90.83%, and 63.26% for 1A; 97.61%, 79.04%, and 60.94% for 2A; and 95.37%, 48.49%, and 42.81% for 4A over three electrolysis cycles. Three key findings emerged from our investigation: First, the resistivity of calcareous sand displayed a three-stage variation pattern, primarily governed by temperature and gas content evolution. Second, the temperature-corrected resistivity model provided reliable saturation data, revealing that electrode-adjacent soil layers exhibited significantly greater saturation reduction compared to intermediate layers. The average saturation variation during a single electrolysis cycle reached 3.2%, 2.6%, and 4.4% for 1A, 2A, and 4A, respectively, in the soil layers near the electrodes, compared to 2.1%, 1.7%, and 3.3% in the middle soil layers under the same current intensities. Third, upon stopping electrolysis, gas redistribution led to decreased saturation in upper soil layers, with lower current intensities more effective in retaining gases within the soil matrix. Based on these findings, an electrolytic influence coefficient for calcareous sand applicable to Archie's formulation is proposed. This study enhances the understanding of the mechanism of electrolysis desaturation and provides a theoretical basis for the effectiveness of electrolysis desaturation on calcareous sand foundations.

Keywords: electrolysis desaturation; calcareous sand; resistivity; liquefaction mitigation; pore gas content

check for updates

Academic Editor: Marco Corradi

Received: 17 May 2025
Revised: 8 June 2025
Accepted: 13 June 2025
Published: 15 June 2025

Citation: Chen, Y.; Zhou, Y.; Chen, R.; Sarajpoor, S.; Xie, X. Electrical Characteristics and Desaturation Effectiveness During Horizontal Electrolysis in Calcareous Sand. *Buildings* **2025**, *15*, 2061. https://doi.org/10.3390/buildings15122061

Copyright: © 2025 by the authors. Licensee MDPI, Basel, Switzerland. This article is an open access article distributed under the terms and conditions of the Creative Commons Attribution (CC BY) license (https://creativecommons.org/licenses/by/4.0/).

1. Introduction

In recent years, calcareous sand has become a primary fill material in land reclamation projects in the South China Sea [1], where these foundations are susceptible to liquefaction during seismic events due to excess pore water pressure accumulation, potentially causing damaging deformations to buildings [2]. The pioneering work of Seed [3] established that soil density, initial stress conditions, and drainage conditions are primary factors controlling liquefaction susceptibility [4]. Calcareous sand primarily consists of aragonite and high-magnesium calcite, which possess a hardness approximately half that of quartz, making the

particles susceptible to crushing [5]. Conventional mechanical approaches for liquefaction mitigation, such as stone columns (SCs) and pile-pinning, have demonstrated effectiveness in terrestrial sandy soils through different mechanisms—SCs primarily enhance drainage, while pile-pinning provides structural reinforcement [6]. However, these methods may exacerbate particle crushing in calcareous sands while simultaneously inducing asymmetric soil responses. Qiu et al. [7] demonstrated that inclination coefficients >0.9 can increase pore pressure by 28–34%, while Okamura et al. [8] established that reducing saturation from 100% to 95% significantly enhances the liquefaction resistance ratio (LRR). Consequently, non-mechanical desaturation methods are proposed for calcareous sand foundations, as they circumvent the destructive impacts of mechanical approaches while effectively improving liquefaction resistance [9–12].

Current research on desaturation methods has demonstrated promising results in liquefaction mitigation. Field tests by Okamura et al. [13,14] revealed that injected gas could remain trapped in natural sand for approximately 26 years, with a desaturation zone forming within a 4 m radius of the injection point. Chen et al. [15] confirmed that electrolysis desaturation could achieve an average saturation degree below 92% after 12 h of treatment, with gas migration occurring both vertically and horizontally. Chen et al. [16] conducted systematic laboratory experiments coupled with numerical simulations to evaluate microbially induced carbonate precipitation (MICP) in calcareous sands. Their research demonstrated that using a cementation solution concentration of 1.14 mol/L at 54.4% relative density with 15 treatment cycles achieved optimal results, reducing permeability coefficients to 2.67×10^{-3} cm/s while developing unconfined compressive strengths reaching 11.37 MPa. However, practical field applications encounter several limitations, including strict microbial viability requirements and temperature controls, complex spatial distribution patterns, and substantial operational expenses associated with multiple treatment cycles. Zeng et al. [17] demonstrated that injecting a solution of calcium nitrate and acetate into the ground could stimulate nitrate-reducing bacteria to produce nitrogen gas and calcium carbonate minerals, achieving desaturation via biogas formation. However, this biological gas generation process exhibits limitations including low gas production rates and high sensitivity to soil pH conditions, resulting in increased implementation costs and environmental constraints. Similarly, air injection faces inherent difficulties in achieving uniform gas distribution [18] After evaluation, electrolysis desaturation is considered the most suitable method for calcareous sand foundations. It generates gas within soil pores without external pressure application, minimizing soil disturbance, while offering the capability to treat foundations beneath existing structures and allowing repeated treatments following electrode installation [19,20]. The relatively low energy consumption makes it cost effective [15,21]. Additionally, the chlorine gas generated during electrolysis can be collected and recycled [22], meeting environmental requirements.

Research on the electrolysis desaturation of calcareous sand has been primarily limited to small-scale tests. Zhang et al. [23] conducted pioneering studies using X-ray CT scanning to investigate the physical processes of electrolysis desaturation. Their work revealed key resistivity characteristics, bubble dynamics, and spatiotemporal evolution of desaturation zones during electrolysis, demonstrating the technical feasibility of horizontal electrolysis in calcareous sand models. Chen et al. [24] employed low-field nuclear magnetic resonance (1H L-F NMR) to elucidate the microscopic mechanisms of horizontal electrolysis desaturation. Their findings demonstrated that electrolysis predominantly discharges free pore water, while the content of bound water—categorized into weakly bound water (physically adsorbed on particle surfaces) and strongly bound water (mechanically immobilized by capillary forces and surface tension)—remains stable throughout the process. This thin, stable layer resists displacement during the electrolysis process and plays a key role in

maintaining particle cohesion. The study also found that rapid bubble generation at high current rates causes temporary pore expansion, with macropores recovering to initial states within 3 h post-electrolysis while meso- and micropore structures remain stable. Zhang et al. [25] conducted integrated experimental and numerical modeling to analyze and validate the expansion patterns of desaturation zones and saturation distribution characteristics, establishing hyperbolic equations to predict the evolution of desaturation zones during electrolysis.

Previous studies on the electrolysis desaturation of calcareous sand foundations have revealed three critical research gaps: (1) inadequate consideration of temperature effects on resistivity measurements during electrolysis, (2) lack of systematic investigation into depth-dependent saturation distribution patterns, and (3) insufficient understanding of post-treatment saturation redistribution. To address these gaps, this study conducted comprehensive horizontal electrolysis tests using a 95 cm × 20 cm calcareous sand column with three successive treatment cycles (1A for 2 h; 2A and 4A for 1 h) at 24 h intervals. This study presents several key advances in understanding electrolysis desaturation for calcareous sand foundations. First, we identify and characterize three distinct stages of resistivity evolution during electrolysis—initial gas-dominated, transitional temperature-influenced, and stabilized equilibrium phases—providing a framework for interpreting resistivity measurements under dynamic electrolysis conditions. Second, we quantify depth-dependent desaturation patterns, demonstrating that the soil layers near the electrodes exhibit 1.5~1.7 times greater saturation reduction (3.2~4.4%) than the middle soil layers (2.1~3.3%) across all current intensities (1A, 2A, and 4A), highlighting the importance of depth-resolved analysis in treatment design. Third, we reveal the saturation behavior after stopping electrolysis, with minimal saturation rebound ($\leq$0.1%) observed during 24 h non-electrolysis intervals, suggesting that achieved desaturation levels remain stable between treatment cycles. Importantly, we demonstrate that lower currents achieve higher gas retention efficiency than higher currents at equivalent gas production volumes, as supported by energy consumption analysis (0.04–0.08 kW·h per cycle at 1A vs. 0.33–0.76 kW·h at 4A), which justifies the strategy of employing multiple low-current electrolysis cycles for energy-efficient desaturation. Furthermore, the derived electrolytic influence coefficient (k) enables the accurate prediction of saturation under electrolysis conditions, enhancing practical applicability. Collectively, these advances provide critical insights for optimizing electrolysis desaturation in calcareous sand, particularly for marine engineering applications where liquefaction mitigation is essential.

2. Experimental Methods

2.1. Experimental Principle

The electrolysis method generates gas within the sand sample without changing the porosity of the sand [26]. Electrolysis of the pore fluid produces bubbles that discharge pore fluid from the soil's pore structure to transform the saturated foundation into the unsaturated state [27]. This process, referred to as electrolysis desaturation, was the focus of this study, which aims to simulate the reclaimed foundations of the South China Sea, where seawater serves as the pore fluid. The chemical reactions during the electrolysis process in this study are as follows:

Anode: chloride ions (Cl^-) are oxidized at the anode to produce chlorine gas (Cl_2):

$$2Cl^- \rightarrow Cl_2 + 2e^- \quad (1)$$

Cathode: water molecules (H_2O) are reduced at the cathode to produce hydrogen gas (H_2) and hydroxide ions (OH^-):

$$2H_2O + 2e^- \rightarrow 2OH^- + H_2 \quad (2)$$

Furthermore, under specific conditions, the electrolyte undergoes the following reactions:

$$Cl_2 + H_2O \rightleftharpoons HClO + HCl \quad (3)$$

$$HClO + NaOH \rightarrow NaClO + H_2O \quad (4)$$

Overall reaction:

$$2NaCl + 2H_2O \rightarrow Cl_2 + H_2 + 2NaOH \quad (5)$$

The current intensity and the soil's resistance jointly determine the interelectrode potential during electrolysis. Zhang et al. [23] conducted X-ray CT scanning analysis on similar calcareous sand samples and observed no significant spatial discontinuities or heterogeneities in particle and pore distributions. Therefore, the calcareous sand foundation can be reasonably assumed to have uniformly distributed pores. Consequently, the sand column resistance (R) correlates with the sand's effective resistivity, as described by Equation (6) [28,29].

$$R = \rho\frac{L}{S} = \frac{U}{I} \quad (6)$$

where L is the length between the electrodes; S is the cross-sectional area; ρ is the effective electrical resistivity; U is the electrical potential between the electrodes; and I is the current passing through the sand column. This experiment employed the voltammetric method to measure the potential difference between graphite felt electrode sheets by testing the constant current in the tested soil layer. The resistivity was calculated according to Equation (6).

Archie [30] examined the relationship between soil parameters and resistivity using different soil samples and cores, and proposed Equation (7) to determine soil resistivity under constant temperature and pressure.

$$\rho = \alpha\rho_w n^{-m} S_r^{-B} \quad (7)$$

where α, m, and B are the empirical parameters related to the soil structure; ρ_w is the resistivity of pore fluid; n is the soil porosity; and S_r is the degree of saturation. Subsequently, Archie's formulation assumes a pure water–electrolyte system, in calcareous sand with saline pore fluid (35‰ NaCl), where the effect of the electrolysis process on empirical parameters related to soil structure is uncertain. Therefore, we can indirectly derive changes in saturation within the bedrock by monitoring changes in resistivity before and after the electrolytic test.

Rhoades et al. [28] confirmed that volumetric water content significantly impacts soil conductivity. On this basis, McNeill [31] proposed the relationship between the resistivity ratios of unsaturated and saturated soil through experimental analysis, as shown in Equation (8).

$$\frac{\rho_{unsat}}{\rho_{sat}} = S_r^{-B} \quad (8)$$

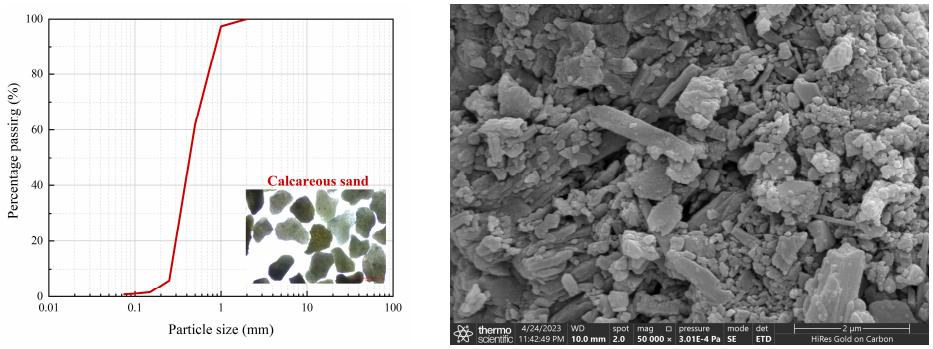
where ρ_{unsat} is the resistivity of the unsaturated soil, ρ_{sat} is the resistivity of the saturated soil, and B is an empirical parameter. During the electrolysis process, the electrical resistivity of the calcareous sand foundation changes due to gas migration and variations in saturation degree. Consequently, monitoring resistivity changes before and after the electrolysis test

can reflect the change in pore gases [32,33]. The change in resistivity of the sand ρ_c can be calculated using Equation (9).

$$\rho_c = (\rho_{unsat} - \rho_{sat})\rho_{sat}^{-1} = \frac{\rho_{unsat}}{\rho_{sat}} - 1 = S_r^{-B} - 1 \quad (9)$$

2.2. Experimental Materials andApparatus

The model test utilized calcareous sand from the South China Sea, and its shape and grading curve are depicted in Figure 1. Basic physical properties of the calcareous sand were determined through laboratory tests. The physical properties of the calcareous sand are detailed in Table 1. To simulate a marine environment, a 35‰ NaCl electrolyte solution was prepared with pure water to reflect the global ocean salinity distribution, which ranges from 34‰ to 36.4‰ [34].



(**a**) (**b**)

Figure 1. Calcareous sand: (**a**) Particle size distribution of calcareous sand, (**b**) Scanning electron microscopy (SEM) images of calcareous sand particles.

Table 1. Physical properties of the calcareous sand.

G_s	C_u	C_c	d_{50} (mm)	e_{max}	e_{min}
2.83	3.46	1.25	0.49	1.05	0.77

As illustrated in Figure 2a, the experimental apparatus consists of an electrolytic cell made from a plexiglass cylinder (95 cm in height and 20 cm in inner diameter) and a large-capacity gas collection bottle. The plexiglass cell provides excellent chemical stability and corrosion resistance, while the gas collection bottle is designed for both measuring the volume of gases released from the cell and for filtration and treatment of chlorine gas generated during electrolysis. The top of the electrolytic cell is sealed with a flange and a silicone gasket, with a dedicated gas outlet connected to the gas collection bottle via a rubber tube. Inside the gas collection bottle, a perforated partition is pre-installed above the water level, on which an activated carbon sachet is evenly spread, ensuring that all incoming gas passes through the activated carbon before displacing the water below into a graduated cylinder for volume measurement. This configuration enables simultaneous quantification of the volume of escaping gases and effective removal of chlorine. After electrolysis, the collected gas is allowed to stand in the gas collection bottle for 24 h, after which potassium iodide–starch test paper is used to detect any residual chlorine, thereby confirming the effectiveness of the gas purification process.

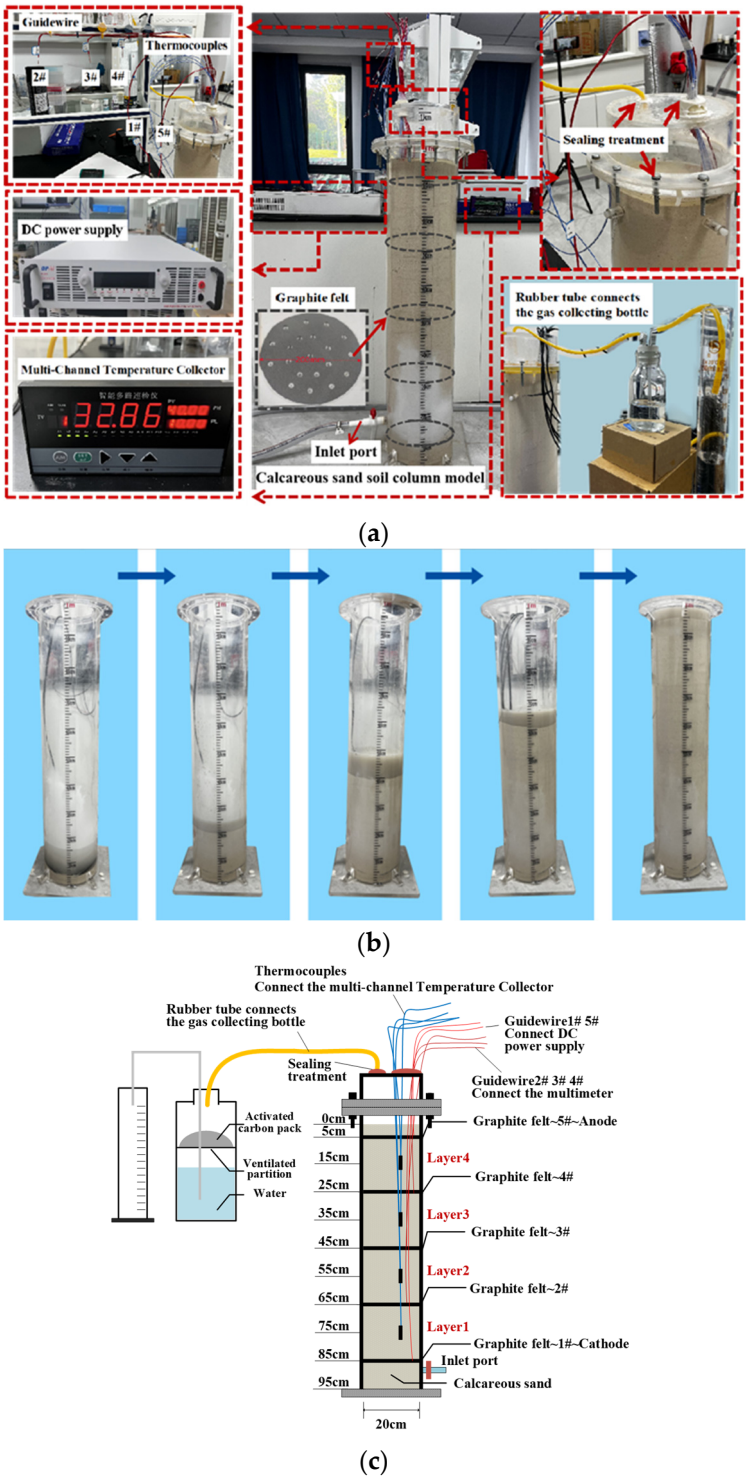


Figure 2. Schematic diagram of the experimental device: (**a**) the set-up of sand column test, (**b**) model preparation, (**c**) schematic diagram.

The electrodes were arranged horizontally within the sample at depths of 5 cm, 25 cm, 45 cm, 65 cm, and 85 cm. They were connected to a direct current (DC) power supply and a multimeter via copper wires. Thermocouples were placed in the sample at depths of 15 cm, 35 cm, 55 cm, and 75 cm, and they were connected to a multi-channel temperature instrument, as shown Figure 2c. All connection wires were securely attached to the inner wall of the model box to prevent any disturbance to the sample. Wire routing holes and air vents are reserved at the top of the model box. All connection wires passed

through the wire routing holes and were secured and sealed with rubber plugs. One end of the rubber tube was inserted into the air vent, while the other end was connected to the gas-collecting bottle. The wire routing holes and air vents were sealed with sealant to maintain an airtight environment within the container. The electrode material used was graphite felt with a thickness of 5 mm and a diameter of 20 cm. Graphite felt is characterized by excellent electrical conductivity, corrosion resistance, high-temperature resistance, and environmental friendliness. Its porous structure provides a large specific surface area, which helps increase the contact area with the electrolyte and the flow of gas within the material, thereby improving the reaction rate of the electrode.

The water pluviation method was employed for sample preparation, as shown in Figure 2b. During sample preparation, the free-fall method was employed, where calcareous sand was uniformly and slowly dropped into sodium chloride solution prepared with degassed water, maintaining the solution level consistently 5 cm above the soil surface. According to soil mechanics principles, this indoor sample preparation method can provide the most conservative estimate of the engineering properties of soils with the same relative density. The dry mass of sand added per 10 cm height was recorded to calculate the relative density, determined to be 45%. To achieve near-complete saturation, degassed sodium chloride solution was maintained at a hydraulic head difference with the sample and slowly permeated from the bottom inlet, flowing upward through the sample while monitoring electrical resistivity changes in each soil layer. The permeation continued until electrical resistivity stabilized, after which the sample remained undisturbed for 12 h to achieve near-complete saturation. In this study, the initial degree of saturation was assumed to be 1.

2.3. Soil Layer Characterization

According to the specimen preparation method described in Section 2.2, the target relative density (D_r) for each soil layer was controlled at 45%. However, self-weight compaction during sample preparation may potentially increase soil density with depth. Based on Terzaghi's one-dimensional consolidation theory [35], we quantified this effect by calculating the compression of each layer and the corresponding variation in relative density based on the soil parameters listed in Table 1. The compression was calculated using Equation (10):

$$\Delta s_i = \frac{a_v \cdot \Delta\sigma_i' \cdot h}{1 + e_0} \tag{10}$$

where i represents the layer number, Δs_i is the compression of soil layer i, a_v is the compression coefficient, $a_v = 0.5\ \text{MPa}^{-1}$, $\Delta\sigma_i'$ is the effective stress increment at the top of layer i, h is the layer thickness (h = 20 cm), e_0 is the void ratio corresponding to 45% relative density (e_0 = 0.924).

The calculated compression and relative density values are presented in Table 2, demonstrating a maximum relative density variation of +0.68%. This observed variation represents only 14~34% of the inherent relative density fluctuations (±2~5%) typically found in homogeneous granular deposits, as documented by Cho et al. [36] in their study of particle shape effects on packing density and stiffness in natural sands. Given that such minor relative density changes would have negligible impacts on both mechanical behavior (with shear strength variations < 1 kPa) and electrolysis test results (showing resistivity changes < 0.5%), the compression-induced density variations in our soil layers can be considered negligible.

Table 2. Calculated compression and relative density variation.

Soil Layer Number	Depth (cm)	Effective Stress $\Delta\sigma'$ (kPa)	Compression Δs_i (mm)	e_i	D_{ri} (%)
4	5~25	0.93	0.048	0.9239	45.04
3	25~45	2.79	0.145	0.9233	45.25
2	45~65	4.65	0.242	0.9227	45.46
1	65~85	6.51	0.339	0.9221	45.68

2.4. Test Conditions

In the electrochemical reaction, the generated hydrogen gas is more stable than chlorine gas, so the cathode, where hydrogen is produced, was placed at the bottom of the sand model, and the anode was placed at the top. Three sets of experimental conditions were designed for this study, as detailed in Table 3. The primary objective of the design was to compare electrical and pore gas changes in calcareous sand with the same total volume of electrolytic gas and electrolysis duration under desaturation conditions.

Table 3. Summary of experimental conditions.

No.		Constant Current (A)	Electrolysis Duration (h)	Electrolysis Count	Non-Electrolysis Duration (h)	Number of Replicates	
						Escaped Gas Collection	Chlorine Monitoring
I_{1A}	1-1	1	2	First	24	3	-
	1-2	1	2	Second	24	3	-
	1-3	1	2	Third	-	2	1
I_{2A}	2-1	2	1	First	24	3	-
	2-2	2	1	Second	24	2	1
	2-3	2	1	Third	-	3	-
I_{4A}	4-1	4	1	First	24	2	1
	4-2	4	1	Second	24	3	-
	4-3	4	1	Third	-	3	-

Each experimental condition was tested with three independent replicates to ensure reproducibility. The repeatability was validated through the following: (1) potential difference measurements, where the maximum deviation was less than or equal to ±5% relative to the maximum recorded potential difference under each current condition; this standard aligns with the typical allowable error margins in geotechnical engineering experiments, which commonly range between ±5% and ±10% depending on measurement conditions; (2) temperature fluctuations, which remained within ±1 °C, consistent with the accuracy specification of T-type thermocouples, and demonstrated less than 0.5 °C variation between replicates, ensuring thermal stability during measurements; (3) derived parameters after model corrections, which exhibited a coefficient of variation (CV) of less than 5%, calculated as $CV = (\sigma/\mu) \times 100\%$, where σ represents the standard deviation of three replicate measurements and μ represents the mean value; the 5% threshold for the coefficient of variation aligns with precision requirements in geotechnical and electrochemical experiments, where CV values below 10% are generally considered acceptable for reliable parameter derivation.

3. Results

3.1. Electrical Characteristics of Calcareous Sand During Electrolysis Desaturation

This section primarily investigated the electrical properties of calcareous sand at different depths during electrolysis desaturation. To evaluate the applicability of Equation

(6) under the uniform pore distribution assumption, we measured the initial resistivity of samples collected from different depths (Figure 3). The observed resistivity variations with depth primarily reflect the inherent heterogeneity of calcareous sand [37], resulting from its characteristic sedimentation patterns. Additionally, minor resistivity fluctuations were detected among replicate samples at identical depths, attributable to temperature effects. Importantly, despite these initial variations, all depth profiles exhibited consistent temporal trends in resistivity evolution. This consistency confirms that Equation (6) remains valid even when accounting for moderate spatial heterogeneity in the soil matrix.

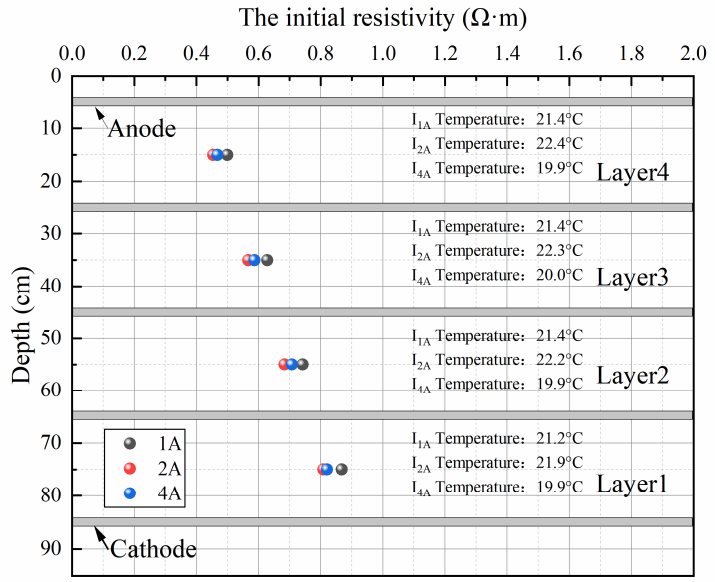


Figure 3. Initial resistivity at different depths: the actual measured deviation across all three replicate trials falls within ±5% of the maximum recorded value and data represent mean values of triplicate experiments.

The distribution of potential differences at varying layers of the sand, as measured in the experiment, is illustrated in Figure 4. According to the experimental data, as the electrolysis time increased, at current intensities of 1A and 2A, the potential differences across various soil layers initially increased and subsequently stabilized. At a current intensity of 4A, the potential differences for soil layers 1–3 initially increased and then decreased, while the potential difference for soil layer 4 exhibited a decreasing trend. Therefore, at lower currents, the changes in potential difference were primarily influenced by variations in pore gas content. The higher the current, the less significant impact of variations in pore gas content on the potential difference. During electrolysis, sand that functions as a three-phase medium facilitated dynamic interactions between liquid and gas within the porous structure. The porosity of calcareous sand remained unchanged despite desaturation via electrolysis. As gas content increased, the proportion of gas-occupied pores rose, leading to higher voltage consumption for the same current passing through a unit area of sand [38]. The greater the current intensity, the higher the concentration of mobile ions in the electrolyte, which increased conductivity and led to a reduction in the voltage consumed.

Figure 5 illustrates changes in temperature during electrolysis. Due to the large amount of data presented in the figure, error bars are not included to ensure clarity and ease of data interpretation. The temperature values shown in the figure represent the averages obtained from three sets of repeated experiments, and the measured resistivity data were calculated as the average of three sets of potential difference test values. The greater the current intensity, the higher the temperature rise. The temperature of the soil layer near

the anode was higher than that near the cathode. At lower currents, the temperature change in the intermediate soil layer was relatively small. Consequently, the change in temperature was related to both current intensity and soil depth. According to Joule's law, the heat generated is proportional to the square of the current. Therefore, a higher current intensity resulted in a greater temperature rise. During electrolysis, oxidation reactions at the anode released heat, while reduction reactions at the cathode generated less heat. This phenomenon typically resulted in higher temperature at the anode compared to the cathode. In the middle section of the soil column, the relatively low current density led to less heat production and thus insignificant temperature changes.

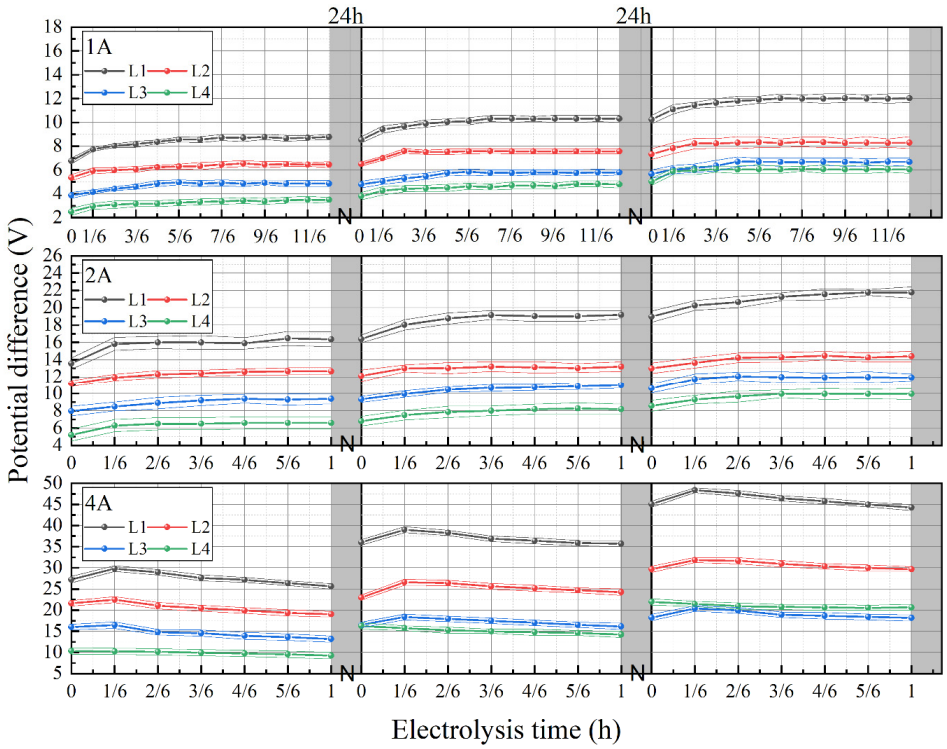


Figure 4. Time-dependent curves of potential difference at different depths under various current intensities: L1 (65–85 cm), L2 (45–65 cm), L3 (25–45 cm), L4 (5–25 cm). The actual measured deviation is within ±5% of the maximum recorded value.

Figure 5 also depicts changes in resistivity throughout the electrolysis process. The relationship between temperature and resistivity changes was analyzed based on experimental measurements. The resistivity change of calcareous sand can be categorized into three stages. In the first stage, the resistivity changes were mainly dominated by gas content, and the resistivity increased. In the second stage, as the temperature increased, resistivity changes were affected by temperature, and the rate of increase in resistivity slowed. In the third stage, resistivity changes were influenced by both temperature and gas content, and the resistivity tended to stabilize. This was attributed to the capacitor's continuous storage and release of charges during the electrolysis, which converted electrical energy into thermal energy and increased the capacitor's temperature. As the capacitor's temperature increased, the activity of electrolytic ions increased, resulting in decreased resistivity. As the gas content increased, the capacitance of the gas was minimal and could often be disregarded, leading to a decrease in total capacitance, and consequently, temperature converged.

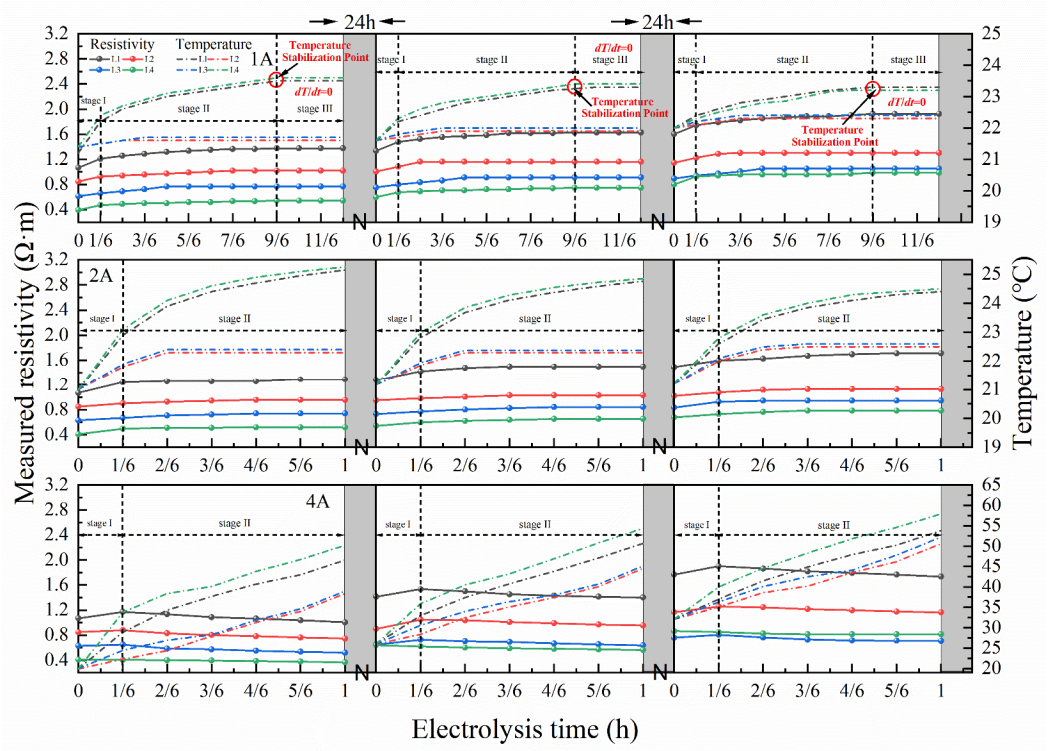


Figure 5. Resistivity between electrodes and temperature during electrolysis: L1 (65–85 cm), L2 (45–65 cm), L3 (25–45 cm), L4 (5–25 cm). The measurement error of the temperature value is within the range of ±0.5 °C.

Figure 5 also illustrates the resistivity variations during electrolysis. Based on experimental measurements, the relationship between temperature and resistivity changes was analyzed. The resistivity evolution in calcareous sand exhibited three distinct stages: In Stage I, resistivity changes were primarily governed by gas content, showing a significant upward trend. This abrupt increase resulted from the rapid accumulation of gas bubbles in the pore structure during initial electrolysis. In Stage II, resistivity growth showed signs of moderation as rising temperature became the dominant factor. The elevated temperature (attributed to the continuous charge storage/release process in the capacitor system, which converted electrical energy into thermal energy) enhanced ionic activity in the electrolyte, thereby slowing the rate of resistivity increase. Under the condition of high current (4A), a negative resistivity growth was observed [39]. During Stage III, resistivity tended to stabilize due to the combined effects of temperature and gas content. As gas content increased (with negligible capacitance), the system's overall capacitance decreased, and temperature stabilized, which was due to the competing effects of temperature and gas accumulation reaching equilibrium [40].

Zhang et al. [23] illustrate resistivity and temperature changes during electrolysis in Figure 6. The experimental material is calcareous sand, and the electrode distance is 6.75 cm. The significant fluctuations in resistivity at the onset of electrolysis suggested capacitor damage. A sudden rise in resistivity was observed when the electrolysis duration exceeded 2 and 4 h. Many large air bubbles were not formed readily. The temperature of the capacitor can exceed 100 °C. A comparison of the two experiments revealed that temperature changes significantly affected the sand's resistivity. As electrode spacing increased, the effect of temperature on resistivity during the electrolysis process was relatively small, resulting in more stable capacitance.

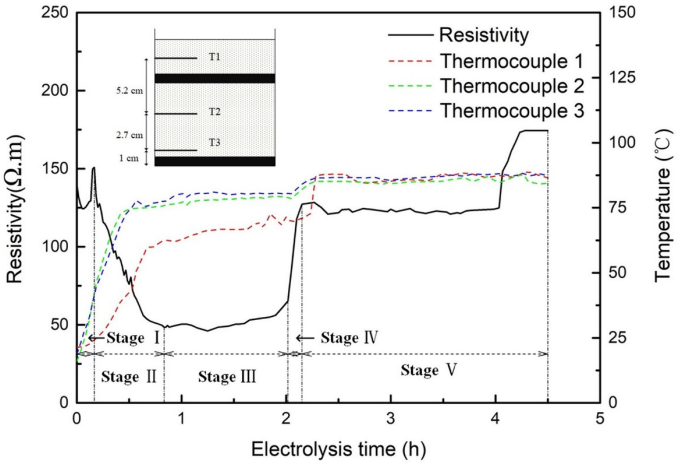


Figure 6. Resistivity between electrodes and temperature during calcareous sand electrolysis [23].

Keller [41] noted that there is a relationship between the resistivity of sand and its temperature, which is expressed as

$$\rho_{T_0} = \rho_T[1 + \alpha(T - T_0)] \tag{11}$$

where ρ_T is the resistivity at temperature T °C, α is the temperature coefficient with a value of 0.025 °C^{-1}, and ρ_0 is the corrected resistivity at the reference temperature T_0 °C. In this study, $T_0 = 20$ °C.

Based on the resistivity values recorded at temperature T °C, the corrected resistivity at the same temperature was obtained using Equation (11). The change in the corrected resistivity was solely influenced by gas content. Figure 7 presents the time-dependent curves of corrected resistivity changes for different soil layers under three experimental conditions.

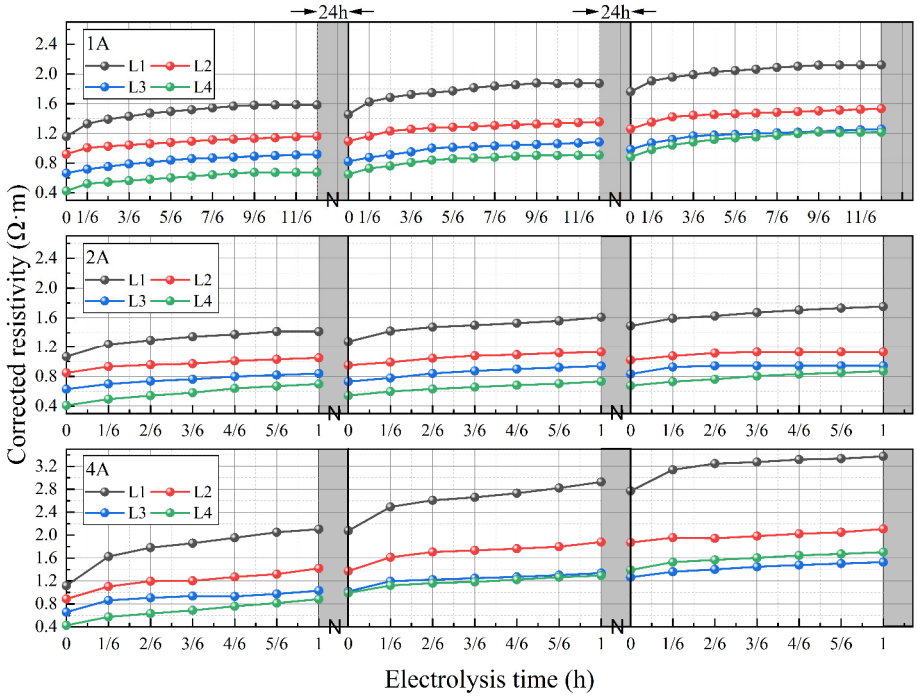


Figure 7. Time-dependent curves of corrected resistivity at different depths under various current intensities: L1 (65–85 cm), L2 (45–65 cm), L3 (25–45 cm), L4 (5–25 cm). the corrected *CV* of resistivity is less than 5% and data represent mean corrected values of triplicate experiments.

Figure 8 illustrates the change in resistivity during electrolysis. In the initial stage of electrolysis at three different current intensities, the rate of increase in resistivity of soil layers 1–3 decreased sequentially. At current intensities of 1A and 2A, the resistivity of soil layer 3 gradually surpassed that of soil layer 2. This suggests that, in the initial stage of electrolysis, the pore gas content near the cathode increased. As electrolysis progressed, the pore gas generated by the bottom cathode electrolysis migrated upwards and gradually accumulated in the soil near the anode. Buoyancy and capillary forces facilitated this upward migration. The pore gas generated by the top anode electrolysis migration diffused and accumulated in adjacent soil layers, resulting in the pore gas in soil layer 3 gradually exceeding that in the underlying soil layer 2.

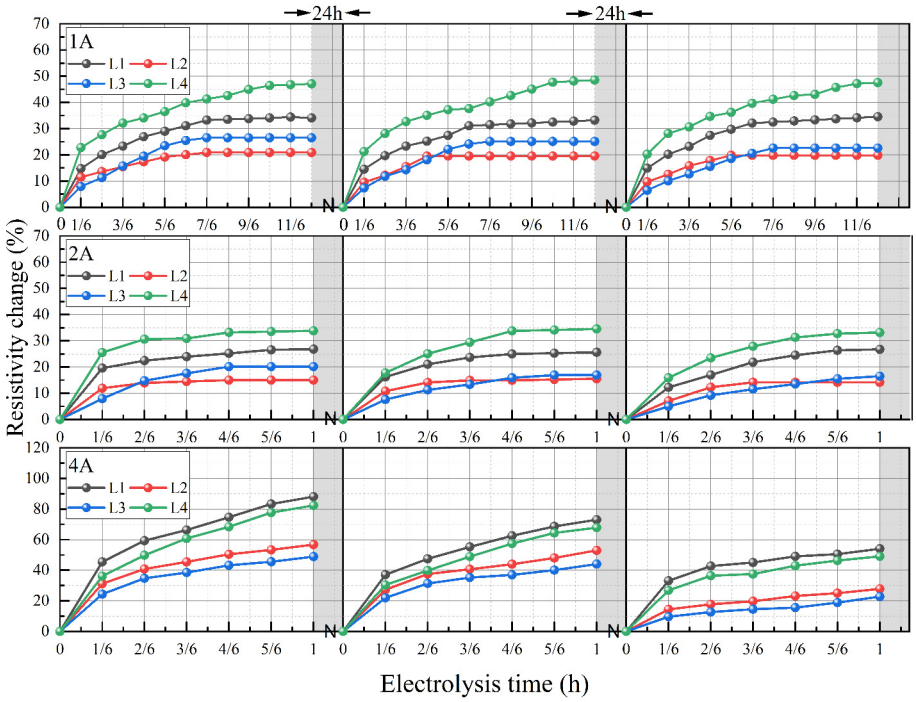


Figure 8. Time-dependent curves of the change in resistivity at different depths under various current intensities: L1 (65–85 cm), L2 (45–65 cm), L3 (25–45 cm), L4 (5–25 cm). The corrected *CV* of resistivity is less than 5% and data represent mean values of triplicate experiments.

At current intensities of 1A and 2A, the increase in resistivity of soil layer 4 near the anode was greater than that of soil layer 1 near the cathode. At a current intensity of 4A, the increase in resistivity of soil layer 1 near the cathode was greater than that of soil layer 4 near the anode. This suggested that gas storage in the upper soil layer was more favorable under low current conditions, as higher currents during electrolysis were more prone to side reactions, with some chlorine gas produced from oxidation dissolving in the pore liquid.

3.2. Saturation Changes in Calcareous Sand Under Electrolysis Desaturation

As governed by Equation (9), the accuracy of saturation inversion via resistivity variation (ρ_c) critically depends on the precise determination of the saturation exponent B. To establish this fundamental relationship isolated from electrolysis effects, a non-electrolytic calibration experiment was implemented through the following standardized protocol:

In the non-electrolytic calibration experiment, calcareous sand specimens at Dr = 45% were prepared by direct mass blending of oven-dried sand and de-aired 35‰ NaCl solution within a Miller box. The test specimens had the same relative density as

the soil column model. Target saturation levels (Sr = 85%, 90%, 95%, 100%) were achieved through precision gravimetric formulation:

$$m_w = \frac{S_r \rho_1}{\rho_2 (1-n)/n} m_s \tag{12}$$

where m_w is the measured mass of salt solution added to achieve target saturation. Sr is the degree of saturation. ρ_1 is the density of NaCl solution at laboratory temperature. ρ_2 is the grain density of calcareous sand determined by pycnometer testing in distilled water, representing the mass per unit volume of the solid skeletal material excluding internal pores. n is the porosity. m_s is the oven-dried mass of the sand specimen.

Resistivity measurements were conducted using a two-electrode method without applied current under strictly controlled isothermal conditions (20 ± 0.5 °C) being maintained. From the fitting of the measured resistivity and saturation using Equation (9), the saturation exponent B of calcareous sand is 7.85 when the relative density is 45%, as shown in Figure 9.

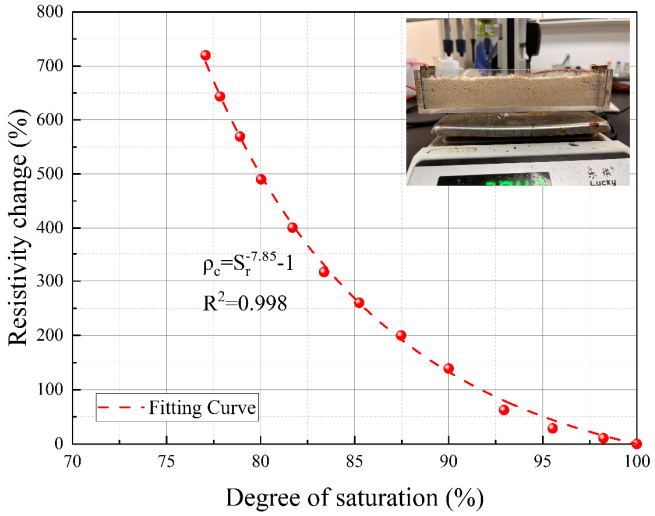


Figure 9. Fitting curve of the relationship between resistivity change and saturation.

The saturation exponent B characterizes the fundamental resistivity—saturation relationship independent of electrolysis processes. As demonstrated in Section 3.1, the temperature-corrected resistivity data during electrolysis effectively decouple thermal effects from saturation changes. The two-stage approach first establishes the intrinsic resistivity–saturation relationship through Miller box calibration and then applies temperature correction via electrolysis tests, which ensures the quantitative validity of using resistivity variation with the fitted *B*-value of 7.85 to characterize saturation changes under electrolysis conditions.

The effect of current intensity on the overall saturation of calcareous sand during electrolysis is depicted in Figure 10. The changes in overall saturation before and after electrolysis of the samples are summarized in Table 4. The overall saturation changes at current intensities of 1A and 2A are relatively close, while the overall saturation significantly decreases at a current intensity of 4A. The greater the current intensity, the rate of change in overall saturation was more rapid in the initial stage of electrolysis but gradually decreased as the electrolysis time extended. This was attributed to increased current intensity leading to a higher generated gas content, which resulted in elevated gas pressure and more pronounced change in saturation levels.

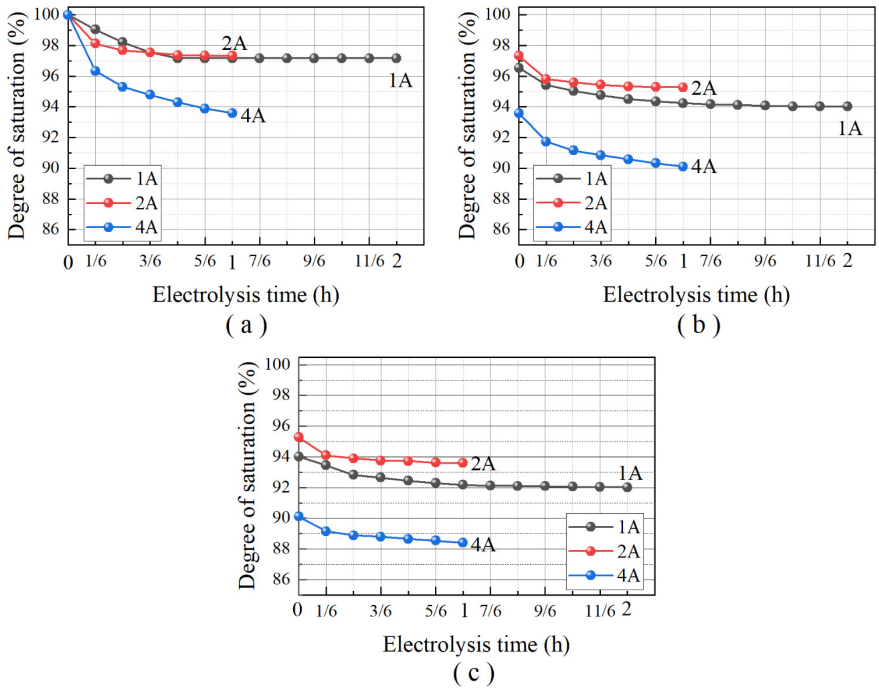


Figure 10. Effect of different current intensities on the saturation during electrolysis: (**a**) first electrolysis, (**b**) secondary electrolysis, and (**c**) third electrolysis, and data represent mean values of triplicate experiments.

Table 4. The overall saturation values before and after the electrolysis.

No.		The Degree of Saturation (%)			
		Start	End	The Change During the Electrolysis Process	The Change Value Between the End of One Electrolysis and the Beginning of the Next Electrolysis
I_{1A}	1	100	96.54	3.46	-
	2	96.63	94.01	2.62	0.09
	3	94.11	92.02	2.09	0.1
I_{2A}	1	100	97.32	2.68	-
	2	97.4	95.27	2.13	0.08
	3	95.35	93.59	1.76	0.08
I_{4A}	1	100	93.59	6.41	-
	2	93.68	90.11	3.57	0.09
	3	90.21	88.40	1.81	0.1

Comparing overall saturation at current intensities of 1A and 2A, after three electrolysis sessions, the overall saturation at 1A current intensity decreased by 3.46%, 2.62%, and 2.09%, while at 2A current intensity, decreases were 2.68%, 2.13%, and 1.76%. When the total gas content produced by electrolysis was equivalent, lower current intensity correlated with more significant saturation changes at the end of electrolysis. The electric current-induced airflow may explain this phenomenon. As the current generated an upward gas flow, it facilitated the escape of gas from the pore structure of the sample. Consequently, higher current intensity resulted in greater gas flow, which allowed a greater volume of gas to escape from the sample. This reduction in retained gas content within the sand pores ultimately led to comparatively smaller changes in saturation levels. In conclusion, reducing the current intensity and increasing the electrolysis duration in electrolysis can enhance the desaturation effect.

As the electrolysis time continues, the rate of overall saturation changes decreases, and multiple electrolysis processes can effectively improve the desaturation efficiency. This is because, during the continuous electrolysis process, the formation of stable gas channels in the sand pore reduced the desaturation efficiency. Multiple electrolysis processes can create new gas channels, thereby enhancing the desaturation efficiency.

The overall saturation changes between the end of one electrolysis and the beginning of the next electrolysis had a maximum value of 0.1% and a minimum value of 0.08%. In the absence of electrolysis, some unstable gas bubbles escaped from the surface of the sand's pore structure, which was possibly due to gas channels formed during the electrolysis process. These unstable gas bubbles within these channels escaped from the sample surface under buoyancy force. This observation is consistent with previous research results, which indicated that after the air injection in soil, only a limited number of air bubbles could escape from the sample [13].

As shown in Table 5, the statistical analysis of saturation differences across current intensities was conducted by calculating mean values and standard deviations from three electrolysis sessions.

Table 5. Statistical analysis of saturation changes at different current intensities.

Constant Current (A)	Mean Saturation Change (%)	Standard Deviation	Coefficient of Variation
1	2.72 ± 0.69	0.69	0.25
2	2.19 ± 0.46	0.46	0.21
4	3.93 ± 2.35	2.35	0.60

The descriptive statistics show two clear patterns in the desaturation process. First, saturation changes vary consistently with current intensity. Second, result variability grows significantly at higher currents. To better understand these patterns, we analyze the complete dataset using boxplots, as shown in Figure 11. The boxplot reveals clear trends in the desaturation process across different current intensities. Saturation changes consistently vary with current intensity, and variability grows significantly at higher currents. At lower intensities, such as 1A and 2A, saturation levels are relatively stable, with narrower interquartile ranges and fewer outliers, reflecting more predictable and uniform desaturation effects. In contrast, the 4A condition exhibits a broader interquartile range, numerous outliers, and a higher coefficient of variation (0.60), indicating less uniform and less predictable results. These findings confirm that lower current intensities, particularly 1A, result in more effective desaturation compared to higher intensities like 2A or 4A, even at equivalent total gas production. This phenomenon can be attributed to gas migration dynamics: higher currents generate gas more rapidly, leading to larger bubbles and continuous gas channels that facilitate gas escape rather than retention within the pore structure. In comparison, lower currents promote more stable gas retention, minimizing preferential channel formation. Collectively, these observations support the conclusion that lower current intensities with longer electrolysis durations are more effective for desaturation treatment, as they enhance uniformity and stability in gas retention within the sand matrix.

Figure 12 presents the saturation time curves of samples at different depths. At a current intensity of 4A, the saturation variation in the soil near the cathode was higher than that near the anode; however, at current intensities of 1A and 2A, the opposite was observed. This is because the larger gas flow generated by the higher current intensity facilitated the formation of gas channels. As gas moved upward more rapidly through these channels, potentially leaving the sample surface, this resulted in a higher saturation near the anode compared to the area near the cathode. In conclusion, gas generated by

electrolysis at a lower current intensity did not readily form gas channels, leading to more efficient gas retention within the sand, which could continue to reduce saturation levels.

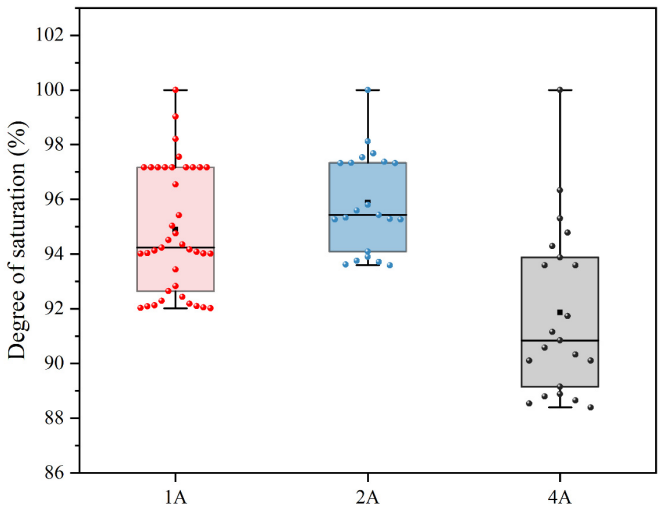


Figure 11. Boxplot of saturation variation under different current conditions.

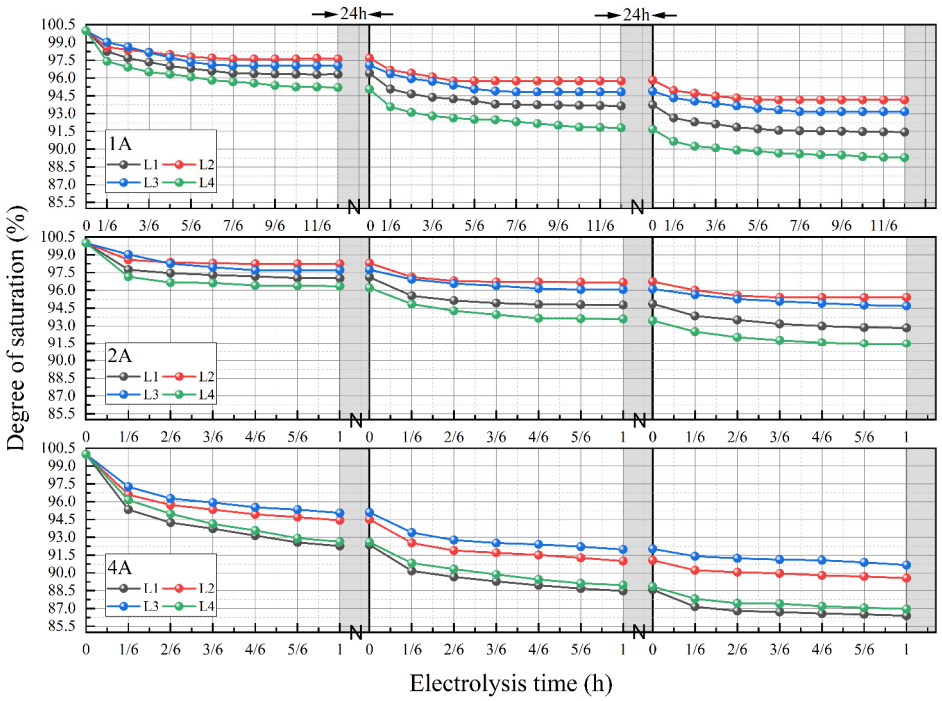


Figure 12. Time-dependent curves of saturation degree at different depths under various current intensities: L1 (65–85 cm), L2 (45–65 cm), L3 (25–45 cm), L4 (5–25 cm). Data represent mean values of triplicate experiments.

The saturation variation in the soil layer near the electrode was more pronounced than that in the middle soil layer, with the average saturation variation during a single electrolysis cycle reaching 3.2%, 2.6%, and 4.4% for 1A, 2A, and 4A, respectively, in the soil near the electrode, compared to 2.1%, 1.7%, and 3.3% in the middle soil layer under the same current intensities. As current intensity increased, the difference in saturation between the soil layer near the electrode and the middle soil layer increased. This discrepancy may arise from the considerable distance between the electrodes. The saturation changes in the soil layers near the electrodes were directly influenced by the current, resulting in a rapid variation in gas migration saturation. As gas migrated upwards under the influence of

buoyancy and diffusion, the moisture in the intermediate soil layer was redistributed among soil particles via capillary action. This redistribution allowed the moisture to maintain a relatively uniform distribution within the soil, thereby slowing saturation changes. A larger current had a greater impact on the saturation changes in the soil layers near the electrodes, and saturation changes in the middle layer were less affected, resulting in more significant differences in saturation across various soil layers. Therefore, current intensity had a significant impact on saturation changes in the soil layers near the electrodes, while capillarity greatly affected the saturation changes in the intermediate soil layers.

Resistivity monitoring following electrolysis cessation revealed distinct spatiotemporal distribution patterns in soil layer saturation (Figure 13; H-0, H-1, H-3, H-6, H-24 correspond to 0, 1, 3, 6, 24 h post-cessation, respectively). The data indicate that during the initial 6 h period (H-1 to H-6), mean saturation changes measured +0.06% for layer 1, +0.05% for layer 2, +0.06% for layer 3, and -0.14% for layer 4, accounting for precisely 60%, 62.5%, 100%, and 100% of respective total variations. Primary saturation adjustments occurred within this initial period (pre-H-6), stabilizing by H-24. Layer 4 exhibited maximum change rates (-0.08%/h during H-0 to H-1), while layer 3 achieved saturation stabilization earliest (at approximately H-3), displaying the characteristic profile: maximum saturation gain in bottom layers, earliest stabilization in intermediate layers, and initial decrease followed by a marginal increase in top layers. This distribution originates from coupled gas–liquid phase transport mechanisms: (1) Bottom layer 1: Significant effective stress promotes bubble migration through free water at reduced velocities from H-0 to H-24, concurrent with sustained free water infiltration, yielding progressive saturation increases. (2) Intermediate layers 2–3: Gas migration comprises ascending gas from underlying strata and local bubbles ascending through free water in these layers, establishing dynamic equilibrium with infiltrating free water around H-3. This results in smaller saturation variations and more rapid stabilization. (3) Top layer 4: Gravity-dominated free water movement (H-0 to H-1) transitions to gas ascending through free water (H-1 to H-6), followed by a late-phase (H-6 to H-24) saturation increase due to bubble coalescence and subsequent escape, along with increased gas solubility driven by system-wide temperature reduction. The complete H-0 to H-24 progression demonstrates complex multiphysics coupling (stress–seepage–thermal interactions) governing fluid redistribution in porous media.

3.3. Theoretical Calculation of Gas Content

During the electrolysis process, we observed the drainage of water from the sand specimens. This phenomenon occurs because the electrolytes within the pores participate in electrochemical reactions, producing gases that displace a portion of the pore fluid, resulting in water drainage. Additionally, the experiments monitored the escape of gases ($V_{escaped}$) from the specimens. According to the law of conservation of mass, the total volume of gases produced ($V_{produce}$) by electrolysis is equal to the sum of the volume of retained gas and the volume of escaped gas. To better understand the mechanism of gas retention within the pores during electrolysis, we compared the produced gas volume, the sand specimen drainage volume, the theoretical retained gas volume (V_a), and the escaped gas volume. The theoretical retained gas volume was determined using Equation (14), which is derived from the resistivity–saturation relationship established in Section 3.2. The saturation degree of sand specimens is primarily determined using this resistivity-based model, as it provides continuous, non-invasive measurements throughout the electrolysis process.

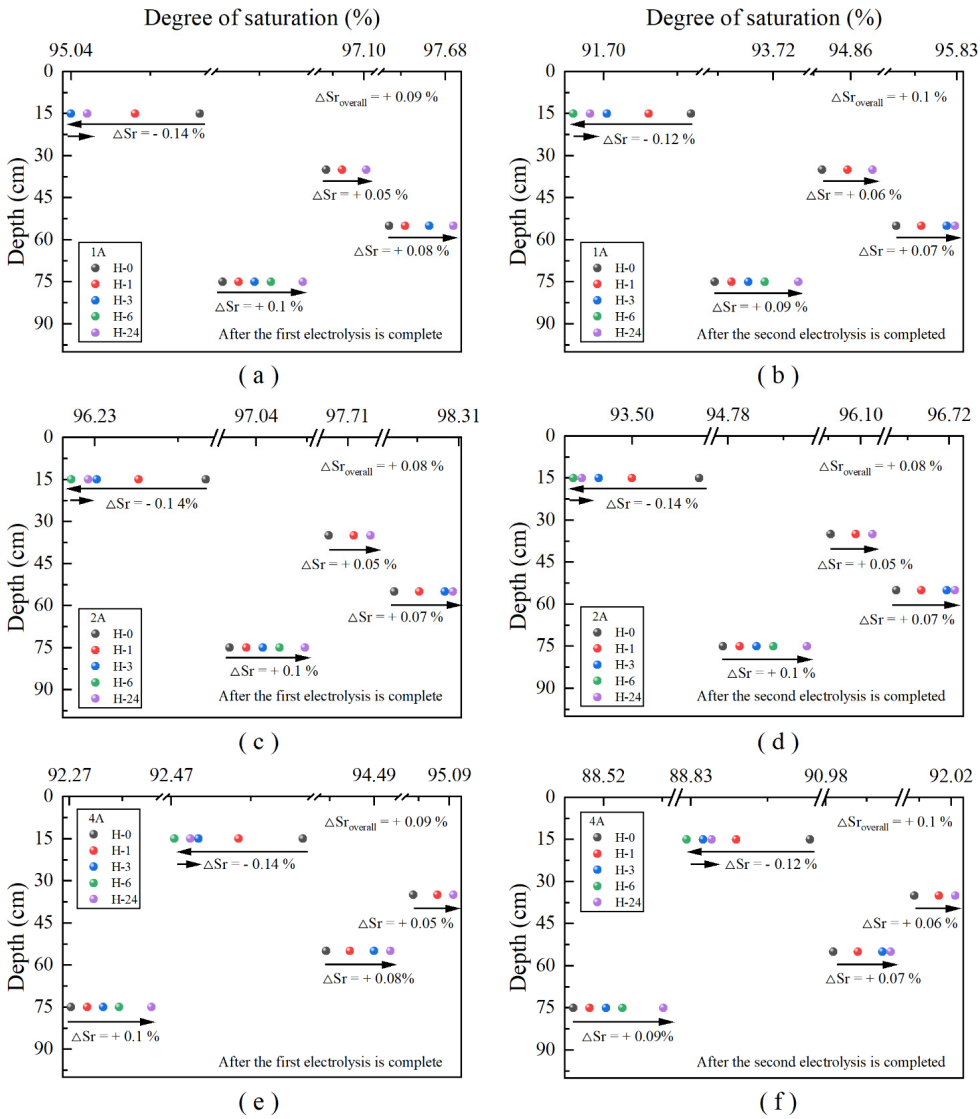


Figure 13. Redistribution of saturation across soil layers after electrolysis cessation at different currents: (**a**) 1A (first cessation), (**b**) 1A (second cessation), (**c**) 2A (first cessation), (**d**) 2A (second cessation), (**e**) 4A (first cessation), (**f**) 4A (second cessation), and data represent mean values of triplicate experiments.

According to Faraday's laws of electrolysis, the amount of substance reduced at the cathode is directly proportional to the current intensity and the electrolysis duration. The volume of gas produced can be calculated as follows [42]:

$$V_{produce} = \frac{It}{z \cdot F} \times 22.4 \tag{13}$$

where $V_{produce}$ is the volume of gas produced by electrolysis, I is the current intensity, t is the electrolysis duration, z is the number of electron transfers (H_2 = 2, Cl_2 = 2), F is the Faraday constant (96,485 C/mol), the molar volume at standard atmospheric pressure is 22.4 L/mol.

Based on the relationship between saturation and gas content, the theoretical retained gas volume based on changes in resistivity can be established as follows [7]:

$$V_a = S_a V_v = (1 - S_r)V_v = (1 - \frac{1}{(\rho_c + 1)^{\frac{1}{B}}})V_v \tag{14}$$

where V_a is the theoretical retained gas volume, V_v is the void volume of the sand (the volume of pore fluid when saturation is 1), S_a is the gas content in the pores, and ρ_c is the change in resistivity of the sand.

Figure 14 illustrates the evolution and comparison of different volume quantities during the electrolysis process, including the volume of gases produced by electrolysis, the sand specimen drainage volume, the escaped gas volume, and the theoretical retained gas volume.

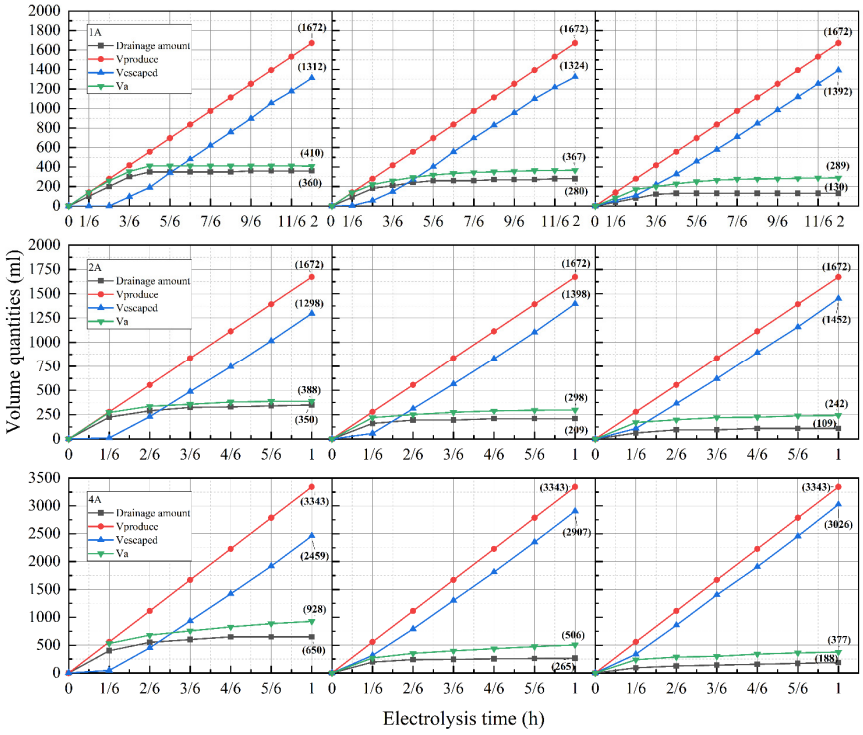


Figure 14. Evolution and comparison of volume quantities during the electrolysis process: data represent mean values of triplicate experiments except for generated gas volume.

When comparing samples subjected to the same electrolysis duration, it was observed that a higher current intensity corresponded with a greater drainage volume. As electrolysis continued, the drainage rate decreased and gradually stabilized. Under the same current, the drainage volume was lower after repeated electrolysis. This was because as electrolysis continued, the gas moved within the pores to form stable gas channels, leading to the release of gas rather than liquid, which resulted in no further change in drainage volume. With repeated electrolysis, the absence of newly formed gas channels caused the liquid content in existing channels to gradually decrease, ultimately reducing drainage volume

The drainage volume recorded after 2 h of electrolysis at a current intensity of 1A was slightly higher than that recorded at 2A for 1 h. Despite the same volume of gas being generated during electrolysis, the volume of drained pore liquid varied. This discrepancy may be because of current intensity on temperature and gas movement speed. The higher the current intensity, the higher the temperature of the sand, and the greater the evaporation of pore liquid, thereby affecting the drainage volume of the sample.

Further analysis reveals that the drainage amount is consistently lower than the theoretical gas storage volume (Va) calculated from resistivity changes. This discrepancy indicates the presence of evaporation, which contributes to the loss of pore liquid during electrolysis. Additionally, the results validate the accuracy of the saturation model used to calculate Va, as it provides a more reliable estimation of the volume of retained gas compared to the directly measured drainage volume.

Further analysis reveals that the drainage amount is consistently lower than the theoretical gas storage volume calculated from resistivity changes. This discrepancy confirms the presence of evaporation during electrolysis, which contributes to pore liquid loss. When comparing the sum of escaped gas volume and retained gas volume with the total produced gas volume, it is evident that the combined volume of escaped gas and theoretically retained gas exceeds the total volume of gases produced during electrolysis. This suggests that evaporation not only reduces the pore liquid content but also contributes to the volume of gas escaping from the sand specimen. Higher current intensities amplify this effect by increasing the temperature, leading to enhanced evaporation rates and accelerated liquid loss. The results validate the accuracy and reliability of the resistivity-based saturation model for calculating retained gas volume, as it provides a more comprehensive estimation compared to the directly measured drainage volume, which fails to account for the evaporation effects.

The retained gas rate during the electrolysis process varied over time, as illustrated in Figure 15. At a current intensity of 1A, the peak gas retention rates during three electrolysis sessions were observed to be 100%, 90.83%, and 63.26%. When the current intensity was increased to 2A, the peak gas retention rates during three electrolysis sessions were observed to be 97.61%, 79.04%, and 60.94%. Further increasing the current intensity to 4A resulted in peak gas retention rates of 95.37%, 48.49%, and 42.81% during the three electrolysis sessions. When the same volume of gas was produced during electrolysis, lower current intensity and longer electrolysis duration yielded higher gas retention rates. Conversely, when the electrolysis duration was constant, gas retention rates did not increase proportionally with increasing current intensity. This was due to a higher current intensity generating a more significant gas flow, leading to greater gas loss from the sample's surface. When the total volume of gas produced during electrolysis was equivalent, a lower current intensity resulted in higher gas retention. Although increasing the current intensity while maintaining constant electrolysis duration increased the total gas content, it concurrently decreased the gas retention rates. Therefore, the gas retention rates did not rise proportionally with increasing current intensity.

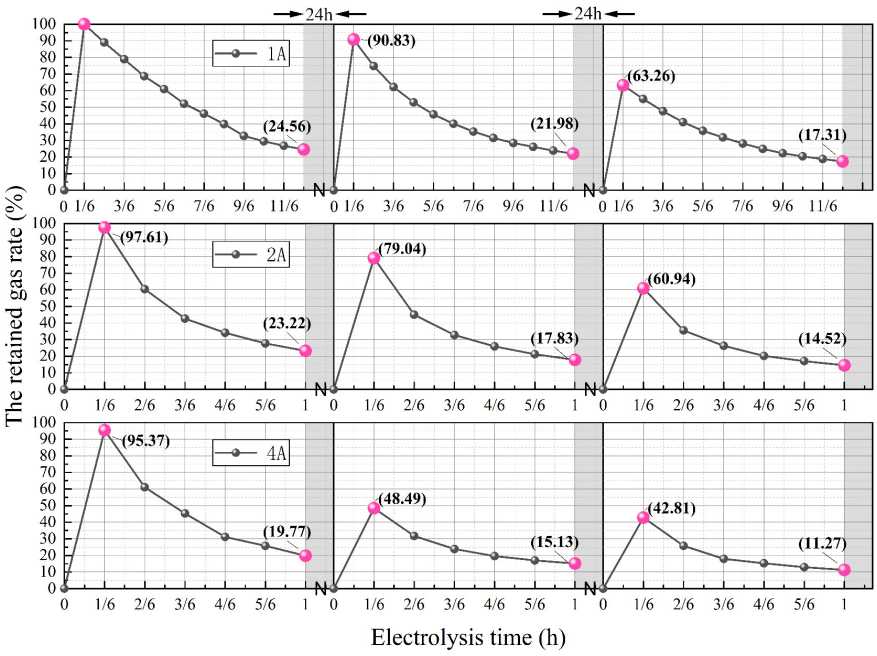


Figure 15. Time-dependent curves of retained gas rate under different current intensities during multiple electrolysis processes: L1 (65–85 cm), L2 (45–65 cm), L3 (25–45 cm), L4 (5–25 cm). Data represent mean values of triplicate experiments.

4. Discussion

In this study, the effectiveness of electrolysis desaturation for calcareous sand foundation treatment was investigated through laboratory tests. Based on the test results and analysis, several key aspects need to be considered for larger-scale implementation.

First, our results demonstrate that the degree of saturation changes significantly near the electrodes while remaining relatively stable in the middle soil layer. As current intensity increases, the saturation difference between the electrode vicinity and middle soil layer becomes more pronounced. Therefore, for larger-scale applications, the optimal electrode spacing should be determined based on this saturation distribution pattern to achieve uniform desaturation effects throughout the treated area.

Second, temperature significantly affects the resistivity during the electrolysis process. Our findings suggest that using lower current intensity leads to more efficient gas retention within the sand, as the generated gas does not readily form channels under these conditions. Thus, temperature control and the application of low current intensity are crucial factors for successful implementation in field conditions.

Third, for foundation engineering in marine environments, environmental protection measures must be implemented to address electrolysis byproducts. In our study, the activated carbon filtration system demonstrated effective chlorine removal, as confirmed by qualitative testing with potassium iodide–starch paper. In the electrolysis desaturation treatment of liquefiable marine foundations, existing chlorine recovery and utilization technologies can be employed to capture and convert chlorine [20], thereby eliminating environmental impacts. The mature application of these technologies can support the environmental sustainability of electrochemical desaturation methods in marine engineering.

This study represents preliminary laboratory investigations. However, when comparing laboratory results to field conditions, implementation faces additional challenges, particularly regarding the durability of desaturation effects under seepage field conditions. Future studies should focus on long-term performance evaluation under actual field conditions to validate the feasibility of large-scale implementation.

4.1. Differential Analysis of the Saturation Exponent

Notably, our *B*-value (7.85) differs significantly from Zhang et al.'s *B*-value (1.549) for calcareous sand [23]. As shown in Table 6, the higher saturation index *B* (7.85) observed in this study can be explained by differences in particle characteristics. First, in terms of particle size, the median particle diameter in this study (d_{50} = 0.49 mm) is larger, leading to larger and more complex pore spaces, which makes the effect of saturation changes on resistivity more pronounced. Second, the lower maximum void ratio (e_{max} = 1.05) and minimum void ratio (e_{min} = 0.77) indicate tighter particle packing. Despite the higher particle density (G_s = 2.83 g/cm^3), the increased number of contact points does not significantly improve pore network connectivity. Additionally, the lower relative density (Dr = 45%) suggests that the sand sample is in a looser packing state. Finally, the difference in pore fluid further impacts the saturation index. This study used 35 ‰ NaCl solution as the pore fluid, whose higher conductivity significantly enhances the conductive ability of liquid bridges, thereby increasing the sensitivity of resistivity to saturation changes and resulting in a higher saturation index *B*. Therefore, the saturation index *B* in Archie's formula for electrolyzed calcareous sand requires calibration through non-electrolytic experiments.

Table 6. The overall saturation values before and after the electrolysis.

Parameter	This Study	Zhang et al. [23]
d_{50} (mm)	0.49	0.33
C_u	3.46	3.55
G_s (g/cm^3)	2.83	2.73
e_{max}	1.05	1.44
e_{min}	0.77	1.02
Dr (%)	45	69.2
Pore fluid	35‰ NaCl solution	Pure water
Test method	Non-electrolytic conditions	Non-electrolytic conditions

4.2. Deviations from Archie's Assumptions in Calcareous Sand

Archie's formulation assumes a pure water–electrolyte system without electrochemical reactions. In calcareous sand with saline pore fluid (35‰ NaCl), two critical deviations emerge: (1) Salinity effect: The initial pore fluid resistivity ρ_w = 0.895 Ω·m, representing an 11-fold reduction compared to Archie's pure water benchmarks (>10 Ω·m). (2) Electrolysis-induced disturbances: The dominant disturbance mechanism arises from chloride redistribution due to Joule heating, where localized thermal gradients generate ion concentration differentials. Therefore, to calibrate the electrolytic influence, we defined the electrolytic influence coefficient k ($k = \alpha n^{-m}$). This coefficient can be determined by comparing a non-electrolytic calibration experiment with an electrolytic calibration experiment.

For the non-electrolytic calibration experiment, as detailed in Section 3.2, the Miller box test yielded the following fitted relationship:

$$\rho_c = S_r^{-7.85} - 1 \tag{15}$$

Convert Equation (15) into the conventional Archie form formula form:

$$\rho_{unsat}^{non-elec} = \rho_{sat}^{non-elec} S_r^{-B} = 0.895 \times S_r^{-7.85} \tag{16}$$

where $\rho_{unsat}^{non-elec}$ is the resistivity of partially saturated specimens, while $\rho_{sat}^{non-elec}$ is the resistivity at complete saturation (Sr = 1), corresponding to the pore fluid resistivity measured as 0.895 Ω·m.

For the electrolytic calibration experiment, the mean values derived from repeated experimental trials of the nine test conditions presented in Table 3 yielded 72 data points characterizing the resistivity–saturation relationship.

As shown in Figure 16a, the relationship curve—between the sand resistivity and the degree of saturation—remained consistent across varying current intensities, demonstrating that current intensity does not affect the correlation between sandstone resistivity and saturation. Building on this current intensity–insensitive relationship, the unified fitting of the sand resistivity to degree of saturation across all current intensities is demonstrated in Figure 16b, with the resulting formula expressed as follows:

$$\rho_{unsat}^{elec} = k\, \rho_{sat}^{non-elec} S_r^{-B} = 4.57 \times S_r^{-7.85} \tag{17}$$

where slope is 4.57, comparing the non-electrolytic calibration experiment, the electrolytic influence coefficient k can be obtained: $k = 4.57/0.895 \approx 5.11$ (95% CI: [4.92, 5.34]), $R^2 = 0.99$, the coefficient of determination indicates a good fit of the model. Therefore, the relationship

between the resistivity measured during the electrolysis process and the saturation degree is as follows:

$$\rho_{unsat}^{elec} = 5.11 \times \rho_{sat}^{non-elec} \, S_r^{-B} \quad (18)$$

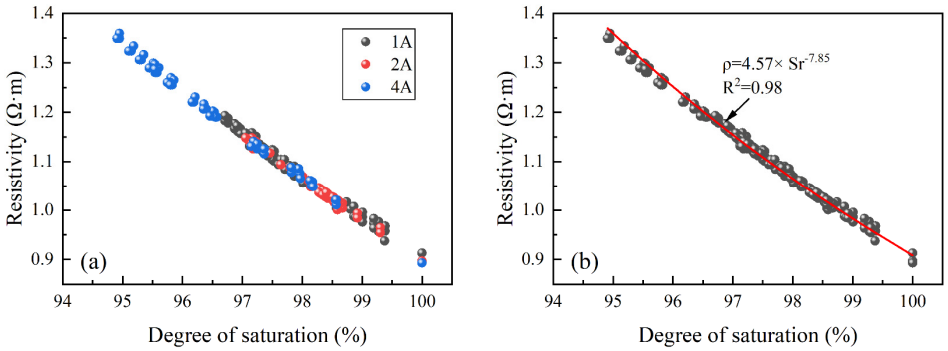


Figure 16. Relationship between resistivity and degree of saturation: (**a**) relationship between resistivity and degree of saturation at different current intensities, (**b**) the fitting curve of resistivity and degree of saturation.

4.3. Analysis of Electricity Consumption

Electricity consumption under different test conditions can be shown by recording the voltage varying across the electrodes during energization. Figure 17 illustrates the variations in measured equivalent resistance and theoretical equivalent resistance under different current intensities and electrolysis cycles. The measured equivalent resistance is obtained directly from recording the voltage and reflects the actual impedance of the electrolysis system during operation, including the effects of temperature and reaction conditions. In contrast, the theoretical equivalent resistance is derived from theoretical calculations with temperature effects corrected, eliminating the temperature interference in the measured results and providing values closer to ideal conditions.

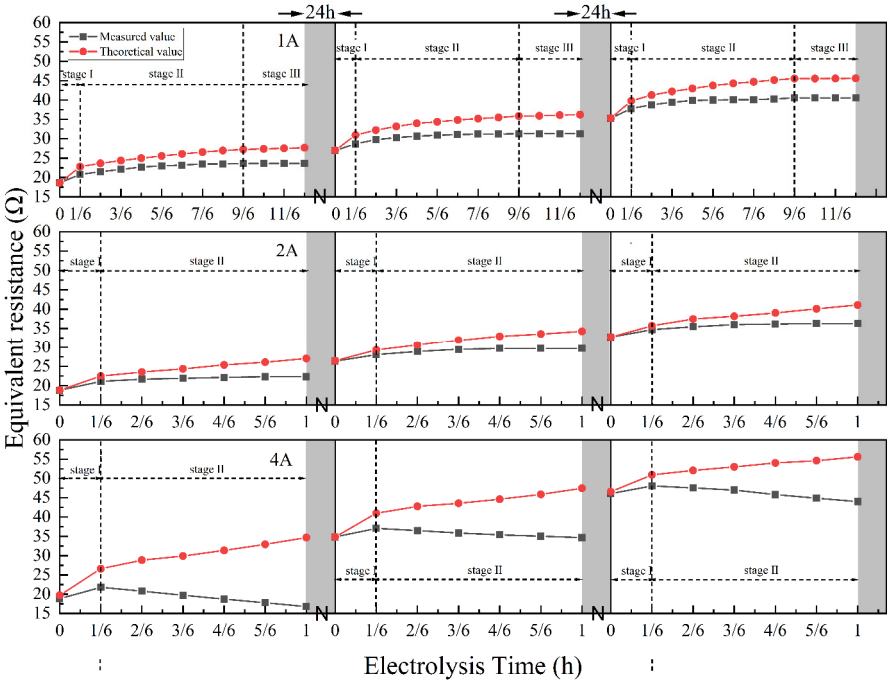


Figure 17. Comparison of measured and theoretical equivalent resistance during electrolysis at different currents and cycles: data represent mean values of triplicate experiments.

By comparing the measured and theoretical equivalent resistance, it is evident that the theoretical values are consistently higher than the measured ones. At lower current intensities, the difference between the measured and theoretical values is smaller, whereas at higher current intensities, the discrepancy increases. Both the measured and theoretical resistance values gradually increase with the number of electrolysis cycles. This behavior can be attributed to the influence of temperature: elevated electrolysis temperatures reduce the resistivity of the electrolyte, leading to lower measured resistance values. As current intensity increases, the heat generated during electrolysis also increases, amplifying the temperature's effect on the measured resistance, which shows a decreasing trend. Furthermore, with more electrolysis cycles, the system cools to room temperature during the intervals between cycles, and the baseline internal resistance of the electrolysis system increases. As a result, the initial equivalent resistance for subsequent electrolysis cycles exhibits closer measured and theoretical values compared to the theoretical value observed at the end of the previous cycle.

Figure 18 illustrates the power variation under different electrolysis conditions. From the data, it can be observed that at 1A, the power is in the range of 0.018~0.04 kW; at 2A, the power increases to 0.07~0.15 kW; and at 4A, it rises significantly to 0.25~0.8 kW. At the end of electrolysis, the total energy consumption for each current intensity, obtained by integrating the power curve under different conditions, is as follows: 1A requires approximately 0.04–0.08 kW·h, 2A requires about 0.09–0.15 kW·h per cycle, and 4A consumes around 0.33–0.76 kW·h per cycle. This indicates that energy consumption increases substantially with higher current intensities. Based on the three stages of resistivity–temperature response discussed in Section 3.1, when $dT/dt = 0$, the electrolyte resistivity stabilizes, indicating that the system has reached thermal equilibrium. Further electrolysis beyond this point would result in diminishing power efficiency. Therefore, to reduce energy consumption, it is recommended to adopt a strategy of using smaller currents and multiple electrolysis cycles. Additionally, the electrolysis process should be stopped when temperature changes stabilize to optimize energy efficiency.

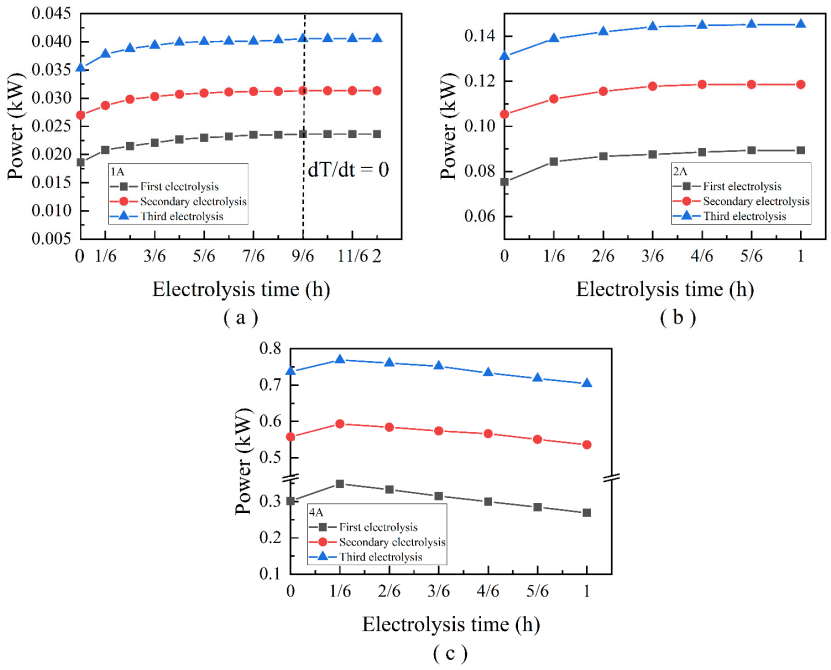


Figure 18. Time-dependent power consumption during electrolysis under varying current intensities: **(a)** 1A, **(b)** 2A, **(c)** 4A. Dnd data represent mean values of triplicate experiments.

5. Conclusions

This study conducted horizontal electrolytic model tests on calcareous sand columns to investigate the variations in resistivity and saturation at different depths of calcareous sand under varying current intensities and electrolysis durations. The primary conclusions are as follows:

1. The resistivity of the calcareous sand column model was influenced by the coupling of temperature and gas content, and its variation process could be divided into three stages. In the first stage, the resistivity changes were mainly dominated by gas content, and the resistivity increased. In the second stage, as the temperature increased, the resistivity changes were influenced by temperature, and the rate of increase in resistivity tended to slow. In the third stage, the resistivity changes were influenced by both temperature and gas content, and the resistivity tended to stabilize.
2. During the electrolysis process, the saturation variation of the soil layer near the electrode was more significant than that of the middle soil layer, which exhibited relatively stable saturation changes. As current intensity increased, the difference in saturation between the soil layer near the electrode and the middle soil layer increased. The saturation redistributed upon cessation of electrolysis. As soil depth decreased, the increase in saturation diminished, and the saturation at the top of the soil decreased.
3. Gas generated by electrolysis at lower current intensity did not readily form gas channels, leading to more efficient gas retention within the sand, which may continue to reduce saturation levels.
4. The reliability of saturation calculations based on temperature-corrected resistivity variations was verified through comparative analysis of electrolysis-induced drainage volumes. For calcareous sand's unique properties, an electrolytic influence coefficient for Archie's formulation was proposed to accommodate electrolysis conditions, establishing a quantitative relationship between resistivity and saturation during electrolysis. This provides the theoretical foundation for saturation prediction in electrolytic desaturation methods.
5. The analysis of the saturation exponent B indicates that Archie's law parameter B is influenced by both the physical properties of calcareous sand and the characteristics of the pore fluid. Therefore, calibration of the B-value is crucial for assessing the saturation of calcareous sand in marine environments.

Author Contributions: Conceptualization, Y.C.; Methodology, Y.C. and Y.Z.; Software, X.X.; Formal analysis, Y.Z.; Investigation, Y.Z.; Data curation, Y.Z.; Writing—original draft, Y.C. and Y.Z.; Writing—review & editing, R.C. and S.S.; Supervision, R.C. and S.S. All authors have read and agreed to the published version of the manuscript.

Funding: This research was financially supported by the National Natural Science Foundation of China (Grant Nos. 52179101, 51679072, and 51879090).

Data Availability Statement: The datasets used and/or analyzed during the current study are available from the corresponding author on reasonable request.

Conflicts of Interest: The authors declare that they have no known competing financial interests or personal relationships that could have appeared to influence the work reported in this paper.

Abbreviations

The following abbreviations are used in this manuscript:

SC	Stone columns
LRR	Liquefaction resistance ratio
MICP	Microbially induced carbonate precipitation
1H L-F NMR	Low-field nuclear magnetic resonance
SEM	Scanning electron microscopy
DC	Direct current

References

1. Wang, X.Z.; Wang, X.; Jin, Z.C.; Zhu, C.Q.; Wang, R.; Meng, Q.S. Investigation of Engineering Characteristics of Calcareous Soils from Fringing Reef. *Ocean Eng.* **2017**, *134*, 77–86. [CrossRef]
2. Xiao, P.; Liu, H.; Xiao, Y.; Stuedlein, A.W.; Evans, T.M. Liquefaction Resistance of Bio-Cemented Calcareous Sand. *Soil Dyn. Earthq. Eng.* **2018**, *107*, 9–19. [CrossRef]
3. Seed, R.B.; Cetin, K.O.; Moss, R.E.S.; Kammerer, A.M.; Wu, J.; Pestana, J.M.; Riemer, M.F.; Sancio, R.B.; Bray, J.D.; Kayen, R.E.; et al. Recent Advances in Soil Liquefaction Engineering: A Unified and Consistent Framework. *Earthq. Eng. Res. Cent.* **2003**, *6*, 1–71.
4. O'Donnell, S.T.; Kavazanjian, E. The Effect of Desaturation on the Static and Cyclic Mechanical Response of Dense Sand. In *IFCEE 2018*; American Society of Civil Engineers: New York, NY, USA, 2018; pp. 232–241. [CrossRef]
5. Wang, X.; Weng, Y.; Wei, H.; Meng, Q.; Hu, M. Particle Obstruction and Crushing of Dredged Calcareous Soil in the Nansha Islands, South China Sea. *Eng. Geol.* **2019**, *261*, 105274. [CrossRef]
6. Asgari, A.; Oliaei, M.; Bagheri, M. Numerical Simulation of Improvement of a Liquefiable Soil Layer Using Stone Column and Pile-Pinning Techniques. *Soil Dyn. Earthq. Eng.* **2013**, *51*, 77–96. [CrossRef]
7. Qiu, H.; Qiu, R.; Luo, G.; Ayasrah, M.; Wang, Z. Study on the Mechanical Behavior of Fluid–Solid Coupling in Shallow Buried Tunnels Under Different Biased Terrain. *Symmetry* **2022**, *14*, 1339. [CrossRef]
8. Okamura, M.; Soga, Y. Effects of Pore Fluid Compressibility on Liquefaction Resistance of Partially Saturated Sand. *Soils Found.* **2006**, *46*, 695–700. [CrossRef]
9. Yegian, M.K.; Eseller-Bayat, E.; Alshawabkeh, A.; Ali, S. Induced-Partial Saturation for Liquefaction Mitigation: Experimental Investigation. *J. Geotech. Geoenvironmental Eng.* **2007**, *133*, 372–380. [CrossRef]
10. He, J.; Chu, J.; Ivanov, V. Mitigation of Liquefaction of Saturated Sand Using Biogas. *Geotechnique* **2013**, *63*, 267–275. [CrossRef]
11. Eseller-Bayat, E.; Yegian, M.K.; Alshawabkeh, A.; Gokyer, S. Liquefaction Response of Partially Saturated Sands. *I Exp. Results. J. Geotech. Geoenvironmental Eng.* **2013**, *139*, 863–871. [CrossRef]
12. Zeybek, A.; Madabhushi, S.P.G. Influence of Air Injection on the Liquefaction-Induced Deformation Mechanisms beneath Shallow Foundations. *Soil Dyn. Earthq. Eng.* **2017**, *97*, 266–276. [CrossRef]
13. Okamura, M.; Ishihara, M.; Tamura, K. Degree of Saturation and Liquefaction Resistances of Sand Improved with Sand Compaction Pile. *J. Geotech. Geoenviron. Eng.* **2006**, *132*, 258–264. [CrossRef]
14. Okamura, M.; Takebayashi, M.; Nishida, K.; Fujii, N.; Jinguji, M.; Imasato, T.; Yasuhara, H.; Nakagawa, E. In-Situ Desaturation Test by Air Injection and Its Evaluation through Field Monitoring and Multiphase Flow Simulation. *J. Geotech. Geoenvironmental Eng.* **2011**, *137*, 643–652. [CrossRef]
15. Chen, R.; Chen, Y.; Liu, H.; Zhang, K.; Zhou, Y.; Xu, S.; Wu, K. In Situ Desaturation Tests by Electrolysis for Liquefaction Mitigation. *Can. Geotech. J.* **2021**, *58*, 1744–1756. [CrossRef]
16. Chen, Y.; Han, Y.; Zhang, X.; Sarajpoor, S.; Zhang, S.; Yao, X. Experimental Study on Permeability and Strength Characteristics of MICP-Treated Calcareous Sand. *Biogeotechnics* **2023**, *1*, 100034. [CrossRef]
17. Zeng, C.; Van Paassen, L.A.; Zheng, J.J.; Stallings Young, E.G.; Hall, C.A.; Veenis, Y.; Van der Star, W.R.L.; Konstantinou, M.; Kavazanjian, E. Soil Stabilization with Microbially Induced Desaturation and Precipitation (MIDP) by Denitrification: A Field Study. *Acta Geotech.* **2022**, *17*, 5359–5374. [CrossRef]
18. Ji, W.; Dahmani, A.; Ahlfeld, D.P.; Lin, J.D.; Hill, E. Laboratory Study of Air Sparging: Air Flow Visualization. *Groundw. Monit. Remediat.* **1993**, *13*, 115–126. [CrossRef]
19. Chen, Y.M.; He, S.K.; Fang, Z.; Jiang, Q. Field Tests on Liquefaction Resistance of Desaturation Measure of Electrolysis. *Yantu Gongcheng Xuebao/Chin. J. Geotech. Eng.* **2017**, *39*, 832–838. [CrossRef]
20. Casagrande, L. Electro-Osmosis in Soils. *Geotechnique* **1949**, *1*, 159–177. [CrossRef]
21. He, S.K.; Chen, Y.M.; Fang, Z. Electrical Characteristics of Electrolytic Desaturation Method for Liquefiable Foundation. *Yantu Gongcheng Xuebao/Chin. J. Geotech. Eng.* **2016**, *38*, 1434–1441. [CrossRef]

22. Ding, J.; Hua, W.; Zhang, H.; Lou, Y. The Development and Application of Two Chlorine Recycling Technologies in Polyurethane Industry. *J. Clean. Prod.* **2013**, *41*, 97–104. [CrossRef]
23. Zhang, Z.; Chen, Y.; Liu, H.; Zhou, Y.; Zhou, X. Resistivity Characteristics during Horizontal-Layered Electrolysis Desaturation of Calcareous Sand. *Eng. Geol.* **2020**, *279*, 105899. [CrossRef]
24. Chen, R.; Chen, Y.; Liu, H.; Cai, X.; Wu, K.; Zhang, Z. Microscopic Mechanism Analysis of Calcareous Sand in Electrolysis Desaturation Using1 H L-F NMR. *Can. Geotech. J.* **2022**, *59*, 1743–1755. [CrossRef]
25. Zhang, Z.; Chen, Y.; Chen, R.; Zhou, Y.; Liu, H. Saturation Characteristics during Horizontal-Layered Electrolysis Desaturation of Calcareous Sand. *Comput. Geotech.* **2022**, *151*, 104938. [CrossRef]
26. Yegian, M.K.; Eseller, E.; Alshawabkeh, A. Preparation and Cyclic Testing of Partially Saturated Sands. *Unsaturated Soils 2006* **2006**, 508–518. [CrossRef]
27. Bergado, D.T.; Balasubramaniam, A.S.; Patawaran, M.A.B.; Kwunpreuk, W. Electro-Osmotic Consolidation of Soft Bangkok Clay with Prefabricated Vertical Drains. *Gr. Improv.* **2000**, *4*, 153–163. [CrossRef]
28. Rhoades, J.D.; Raats, P.A.C.; Prather, R.J. Effects of Liquid-phase Electrical Conductivity, Water Content, and Surface Conductivity on Bulk Soil Electrical Conductivity. *Soil Sci. Soc. Am. J.* **1976**, *40*, 651–655. [CrossRef]
29. Samouëlian, A.; Cousin, I.; Tabbagh, A.; Bruand, A.; Richard, G. Electrical Resistivity Survey in Soil Science: A Review. *Soil Tillage Res.* **2005**, *83*, 173–193. [CrossRef]
30. Archie, G.E. The Electrical Resistivity Log as an Aid in Determining Some Reservoir Characteristics. *Trans. AIME* **1942**, *146*, 54–62. [CrossRef]
31. McNeill, J.D. Use of Electromagnetic Methods for Groundwater Studies. *Geotech. Environ. Geophys.* **1990**, *1*, 191–218. [CrossRef]
32. Waxman, M.H.; Smits, L.J.M. Electrical Conductivities in Oil-Bearing Shaly Sands. *Soc. Pet. Eng. J.* **1968**, *8*, 107–122. [CrossRef]
33. Abu-hassanein, Z.S.; Benson, C.H.; Blotz, L.R. Electrical Resistivity of Compacted Clays. *J. Geotech. Eng.* **1996**, *122*, 397–406. [CrossRef]
34. Helm, K.P.; Bindoff, N.L.; Church, J.A. Changes in the Global Hydrological-Cycle Inferred from Ocean Salinity. *Geophys. Res. Lett.* **2010**, *37*, 2–6. [CrossRef]
35. Karl, T. *Theoretical Soil Mechanics*; John Wiley & Sons: New York, NY, USA, 1943.
36. Cho, G.-C.; Dodds, J.; Santamarina, J.C. Particle Shape Effects on Packing Density, Stiffness, and Strength: Natural and Crushed Sands. *J. Geotech. Geoenvironmental Eng.* **2006**, *132*, 591–602. [CrossRef]
37. Kherif, O.; Robson, S.; Harid, N.; Thorpe, D.; Stivanello, S.; Haddad, A. On the Impact of Soil Resistivity Measurement and Modelling on Grounding Performance. In Proceedings of the 2022 36th International Conference on Lightning Protection, Cape Town, South Africa, 2–7 October 2022; pp. 379–382. [CrossRef]
38. Chen, R.; Hu, Y.; Chen, Y.; Zhou, Y. Effect of Electrolysis Desaturation Treatment on Micro-Structure of Liquefiable Silica Sands. *Bull. Eng. Geol. Environ.* **2024**, *83*, 285. [CrossRef]
39. Pereira, O.C.N.; Bertonha, A.; de Freitas, P.S.L.; Silvano, C. Development and Calibration of an Electrolytic Cell for Ion Determination in a Soil Solution. *Acta Sci. Technol.* **2015**, *37*, 189. [CrossRef]
40. Rittirong, A.; Shang, J.Q.; Mohamedelhassan, E.; Ismail, M.A.; Randolph, M.F. Effects of Electrode Configuration on Electrokinetic Stabilization for Caisson Anchors in Calcareous Sand. *J. Geotech. Geoenvironmental Eng.* **2008**, *134*, 352–365. [CrossRef]
41. Keller, V. *Electrical Methods in Geophysical Prospecting*; Pergamon Press: Oxford, UK, 1966; p. 155.
42. Jensen, W.B. Faradays Laws or Faradays Law? *J. Chem. Educ.* **2012**, *89*, 1208–1209. [CrossRef]

Disclaimer/Publisher's Note: The statements, opinions and data contained in all publications are solely those of the individual author(s) and contributor(s) and not of MDPI and/or the editor(s). MDPI and/or the editor(s) disclaim responsibility for any injury to people or property resulting from any ideas, methods, instructions or products referred to in the content.